AIAA Journal
Vol. 59, No. 3, March 2021

Effect of a Rotating and Swept Wingtip on Streamwise Gust Alleviation

Juhi Chowdhury* and Matthew J. Ringuette†
University at Buffalo, State University of New York, Buffalo, New York 14260

https://doi.org/10.2514/1.J059690

Dynamic effects of wing planform changes are investigated with the goal of gust alleviation. Force measurements are done on a low-aspect-ratio high-angle-of-attack translating wing having a rectangular planform that incorporates a moving tip with in-plane rotation and sweep. To create streamwise gusts, the wing is towed in a water tank from constant motion to a new velocity that is 50% higher ("step-up") or lower ("step-down") through ramp distances of 1, 3, and 6 chords traveled. The tip panel is rotated inward for the step-up cases to lower the gust lift peaks and outward for step-down gusts to mitigate the lift lost. The actuation cases are compared using the unsteady C_L with two reference geometries (pre- or post-gust wing shapes). In most cases, actuation yields better gust-force change for Æ = 2 than Æ = 4, due to the greater change in wing planform. The actuation timing also alters the details of the force recovery. Furthermore, an impulse metric shows that inward tip actuation can mitigate the gust-impulse change by as much as 38% and outward tip actuation by 84%. A superposition of the individual effects of the actuation and gust is tested against the cases of actuation during gusts.

I. Introduction

The goal of this work is to test whether a moving-wingtip surface that employs in-plane rotation and sweep can aid in mitigating the lift changes from simplified step-up and step-down streamwise gusts. The rotating tip surface, referred to here as a tip panel, dynamically changes the wing planform. The panel is deployed on a low-aspect-ratio translating wing at a high angle of attack α. The long-term application of this research is to develop a method of flow control for unmanned aerial vehicles (UAVs) to employ for gust alleviation or maneuvers.

For wings in unsteady translation at high α, dynamic stall will occur for which the flow separates and a leading-edge vortex (LEV) forms that yields large lift then sheds [1,2]. Taira and Colonius [3] examined tip effects by performing numerical simulations of translating wings with aspect-ratio Æ values of 1 to 4 at large α starting from rest. They showed that tip vortex (TV) downwash lowers the wing lift coefficient, C_L, which progresses as the Æ becomes smaller and the TV influence increases. At Æ = 1, the LEV remains attached due to the dominant TVs; but for higher Æ, this is only true near the wingtips and the inboard LEV lifts off into an arch shape and sheds. Jardin et al. [4] similarly found that the TV promotes LEV attachment for simulations of flapping wings in translation. For further recent work on the forces and flow structure for finite-Æ wings in unsteady translation, see the work of Stevens et al. [5]. Here, we consider Æ = 2 and 4 wings to ensure that inboard LEV shedding will occur, and we observe how the moving tip panel alters the C_L.

Several studies have shown that the LEV is attached for low local Rossby numbers Ro for unsteady rotating wings; this is also in the context of Æ effects, e.g., Refs. [6,7]. The low-Æ rotating tip panel examined here is superimposed on the main-wing translation, for which the advance ratio J that characterizes wing translation versus rotation is also important. Section II.C discusses this and leverages the rotating-wing study of Harbig et al. [8] for varying J.

The moving tip panel studied here incorporates aft sweep along with rotation. For unswept, translating rectangular wings, the LEV and TV are distinct [9,10], but sweep can facilitate an LEV–TV connection [11], yielding outboard vorticity transport and delaying both the LEV shedding and peak C_L [3]. With added flapping (lateral rotation about the root), the wing produces a spanwise vorticity gradient, and sweep can enhance spanwise flow aiding in LEV attachment [12,13]. Klaassen van Oorschot et al. [14] performed tests on actual bird wings with either fixed, aft sweep outboard or the sweep reduced and area increased by extending the wing in a freestream flow or for steady revolving. Sweep produces a larger $C_{L,\max}$ at a higher α in the freestream flow; but for revolving, the extended wings generate greater C_L. Nikolic [15] and Lee and Pereira [16] employed half-delta-wing (swept) tip shapes, also referred to as strakes. Depending on the main-wing and strake orientations, the results showed increased C_L and maximum lift-to-drag ratio, likely due to strake vortex lift. Although this research was done for lower $\alpha \leq 25$ deg and a steady freestream versus the high-α unsteady conditions of the present work with variable tip geometry, it shows that such tip shapes can improve performance.

Prior research has also been done on dynamically changing wing shapes. For example, Reynolds et al. [17] showed that a steppe eagle quickly lowers ("tucks") its wings below its body in reaction to a headwind gust followed by some disturbance like a downdraft that produces a drop in lift. The tucking is likely the response of muscle tension to a suddenly reduced wing loading, but they speculate that it could also be a mechanism for damping the gust perturbation. Wang et al. [18] used direct numerical simulation to study slow-flying bats, and they showed that a dynamic increase in wingspan during flapping, compared to a fixed-span case, produces greater lift and efficiency by enhancing the LEV strength, in addition to the effect of the larger wing area. For additional discussions on the forelimb adaptations of bat and bird wings and potential inspiration for robotic drones, see Ref. [19].

Considering more simplified engineering approaches, recently, Joshi et al. [20] showed when the tip bends dynamically toward the suction side of a translating wing, it enhances C_L due to stabilization of the LEV. Building off the work of Wibawa et al. [21], Steele et al. [22] investigated fast spanwise retraction of vertically mounted wings towed at constant α in water, and they found variations in the vortex structure and energy transfer to or from the flow with different tip geometries. Di Luca et al. [23] designed and fabricated a bird-inspired morphing wing with the outboard portions consisting of multiple artificial feathers that when fully extended, produce outboard sweep,

---

Presented as Paper 2020-2045 at the AIAA Scitech 2020 Forum, Orlando, FL, January 6–10, 2020; received 10 April 2020; revision received 25 September 2020; accepted for publication 27 November 2020; published online 27 January 2021.

*Ph.D. Student, Department of Mechanical and Aerospace Engineering, 211 Bell Hall. Student Member AIAA.

†Associate Professor, Department of Mechanical and Aerospace Engineering, 211 Bell Hall. Senior Member AIAA.

or by rotation inboard, decrease the span and lower the area by 41%. The expanded wing provides greater time-averaged C_L and maneuvering capability, whereas retraction reduces the drag coefficient for higher speed. Also, asymmetric actuation can be used for roll control. A similar discrete (feather) wing structure was studied by Hui et al. [24] for its effect on the induced drag from modification of the tip flow at various angles of attack. However, this wing deforms from the leading edge, and the measurements are taken at four static morphing angles (leading-edge sweep). Di Luca et al.'s [23] variable wing geometry shares similarities with that of the present study; however, we employ a rigid wingtip panel and examine the unsteady forces.

Regarding streamwise gusts, here, the focus is on simple nonperiodic changes in velocity. Experiments have shown that using a moving model with respect to a constant (or zero) freestream velocity to produce a gust-like interaction is equivalent to employing a stationary wing in a wind tunnel with matching relative time-varying freestream-velocity changes, provided that the buoyancy effects from this accelerating freestream and the wing-model inertial loads for the moving-wing case are accounted for [25]. Mulleners et al. [26] conducted experiments on an $\alpha = 30$ deg flat-plate wing, and they compared the LEV and trailing-edge vortex (TEV) development and C_L decay for 1) a starting flow and 2) a streamwise acceleration from a fully developed state at constant velocity to a final velocity 50% higher than the initial wing velocity. They found that after the initial startup, both cases are similar in terms of time-varying flow and C_L variations and decay. Marzanek and Rival [27] studied a nonslender delta wing at $\alpha = 20$ and 30 deg accelerating over $1c$–$6c$ to a 50% faster speed from a constant motion to emulate a headwind gust; c is the chord length. For $\alpha = 30$ deg, they found sensitivity to the acceleration rate: e.g., for the $1c$ case, it exhibits high sustained C_L associated with a favorable pressure gradient and flow separation with subsequent reattachment.

The objective of the current paper is to examine how a rotating tip panel with aft sweep affects the C_L for a rectangular wing experiencing streamwise gusts, with the goal being gust mitigation. A schematic given in Fig. 1 presents an overview of this study. Two main questions are considered:

1) To what level can the lift increase from a headwind gust be reduced via inward panel rotation?

2) How effective is outboard panel rotation at recovering the lift lost during a tailwind gust?

To address questions 1 and 2, simple step-up and step-down streamwise gusts are tested, respectively, where starting from a constant velocity, the wing accelerates or decelerates, respectively, to a new higher/lower constant velocity. Experiments are done in a water towing tank, and the wing lift is measured using a force transducer. The parameters varied include the gust acceleration, panel actuation timing, and main-wing $\mathcal{AR}$. The moving-panel results are compared with two reference cases having fixed planforms at the extremes of the panel actuation: the main wing with no tip panel deployed ("rectangular" wing), and a fixed tip panel fully extended outward with constant sweep ("static sweep").

II. Experimental Setup and Methods

A. Facility and Wing Model

The facility is a 4 m × 1.5 m × 1.1 m glass-walled water towing tank (Fig. 2a). It is open at the top, and the bottom and side walls are supported by a steel frame that elevates it by 1 m for imaging from underneath. Above the tank is an additional frame of extruded-aluminum beams, and four cross beams support a 3 m-long brushless linear stage (H2W Technologies DRS-120-08-006-01-EX) for towing models. A tray is installed adjacent to the stage that supports the cable bundle attached to the stage's carriage and that of the wingtip actuation motor, giving smooth cable travel as the carriage moves. A Galil DMC4040 controller employing encoder feedback provides coordinated programmable motions for the linear stage and the tip panel. The position accuracy of the linear-stage encoder is rated at 1 μm; however, maximum deviations of about 100 μm, or $\sim 0.1\% c$, occur during the gust motions.

The main wing is made from two carbon-fiber composite sheets with thicknesses of 3.18 and 0.79 mm, with a chord length of $c = 81$ mm. A cavity is machined out of the thicker plate to allow room for the actuation mechanism and retracting tip panel; the two plates are glued together with marine epoxy to form the complete wing with a 3.97 mm thickness. The rotating tip panel is a 1.59-mm-thick carbon-fiber composite plate cut into an approximately 1/8-circle shape, the apex of which is pivoted at the leading edge and tip corner of the main wing via a binding barrel (Fig. 2b).

The tip panel is rotated using a small motor, called the tip motor (brushed DC servo motor, Micromo model 2642W012CXRIE3-1024L+26A 16:1+MG26, with 65536 encoder counts per revolution), that is mounted on a vertical aluminum plate above the free surface, which also supports the main wing. A stainless-steel control rod connects with a rotational joint to an arm collared on the tip-motor shaft (see Fig. 2b). The rod passes down through the wing cavity, and

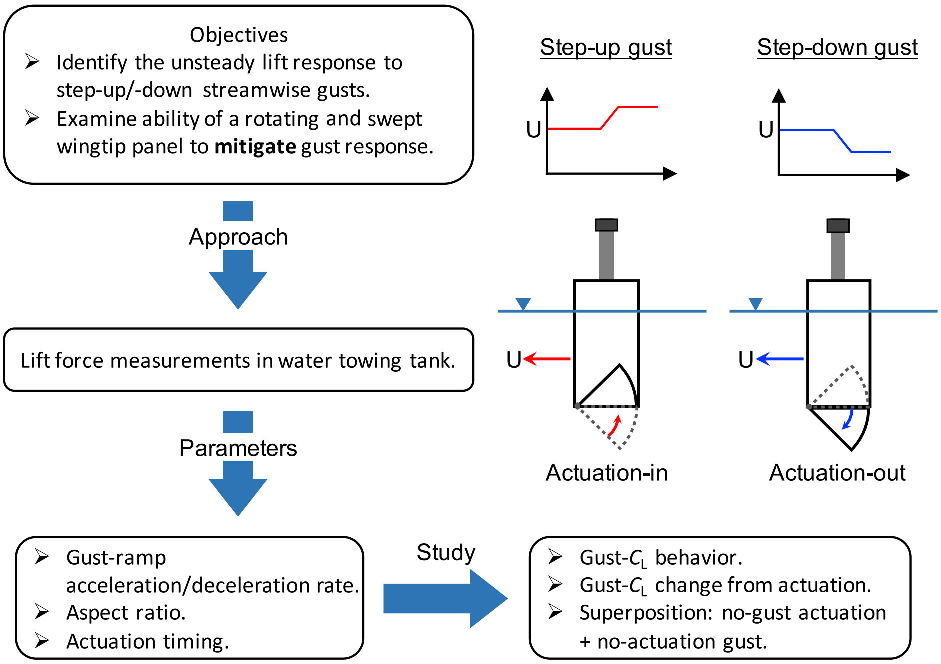

Fig. 1 Research overview for the present paper.

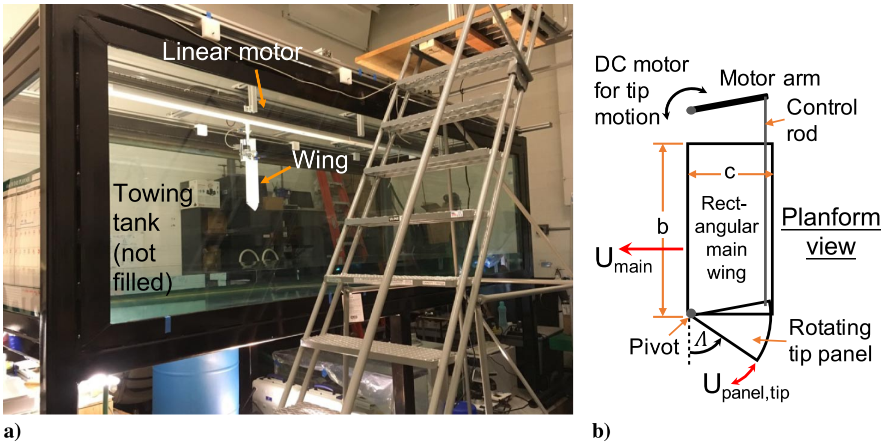

Fig. 2 Experimental setup: a) towing-tank facility, indicating the wing and linear motor; and b) schematic of the wing, with the tip-panel actuation mechanism and wing velocities.

it connects at its lower end to the aft/inboard corner of the pivoted tip panel, also with a rotational joint. The control rod connection to the arm is 68.6 mm from the center of the tip-motor axle, which is approximately the same distance between the tip-panel pivot point and its connection to the rod. Therefore, the panel rotates with the tip motor via the rod, with a nearly one-to-one conversion. Some part of the tip panel is always inside the main wing, even when fully extended; the exposed panel has an average radius of 73 mm from the exposed panel apex. The sweep angle between a line parallel to the main-wing leading edge (LE) and the panel LE is Λ (Fig. 2b), and the angle between the tip edge of the rectangular main wing and the panel LE is $(90\ \text{deg} - \Lambda)$. Using the latter angle, 46.72 deg of motor rotation yields 45 deg of exposed tip rotation. The tip panel can completely retract into the main wing ($\Lambda = 90\ \text{deg}$) or fully extend, giving $\Lambda = 45\ \text{deg}$. The panel rotational velocity is verified using 240-frame-per-second movies of the panel motion. The angular position of its LE over time is determined from still images using Gimp software. The manual edge finding incurs some error, but it shows that the average angular panel velocity from the images is within 0.3% of the motor velocity.

B. Force Measurements

The lift force is measured using a six-axis ATI Gamma force/torque sensor attached between the linear-stage carriage plate and the wing's sting support. The Gamma signals are acquired with a 16-bit National Instruments Data acquisition card (PCIe-6323) via LabVIEW after receiving a trigger signal from the motion controller, and they are sampled at 1 kHz. For each case, $N = 10$ runs are taken both in water and air; the latter allow the model inertial forces to be subtracted off, leaving the fluid-dynamic forces of interest. The transducer measures a nonzero static force (maximum 0.2 N), which varies along the length of the linear motor. This is likely due to subtle variations in the parallel alignment of the stage's dual rails, transmitting stress through the carriage attachment plate to the transducer. This force is very repeatable and is subtracted off via the air runs. MATLAB is used for data processing, and the mechanical vibrations and noise of the system are analyzed from strike tests as well as air and water runs by estimating the power spectral density. A third-order low-pass Butterworth filter with a 4 Hz cutoff frequency is applied to the data, which retains the flow-related forces while removing most of the vibration contributions. After filtering, all runs are aligned in time using the start times found via a threshold of force signal change, the air and water runs are separately averaged, and then the air results are subtracted out.

The Gamma uses the ATI SI-32-2.5 calibration, and its accuracy is checked via static tests with precision weights for forces of ~0.2–2 N, covering the range of the experiment; the results are within 1.5% of the calibration. For a given case, the random uncertainty in the average lift coefficient $\delta C_L(t)$ is computed at each time instant using the precision error of the mean from the run-to-run variations for both water and air measurements, $\delta C_{L,\text{water/air}}(t) = t_{\nu,0.95}\sigma_{\text{water/air}}(t)/\sqrt{N}$, where $t_{\nu,0.95}$ is the Student's t distribution for a 95% confidence level with $N - 1$ degrees of freedom, and the sample standard deviation is σ. Overall, the mean lift coefficient with its precision error for each case is $\bar{C}_L(t) \pm \delta C_L(t) = (\bar{C}_{L,\text{water}}(t) \pm \delta C_{L,\text{water}}(t)) - (\bar{C}_{L,\text{air}}(t) \pm \delta C_{L,\text{air}}(t))$.

Figure 3 shows two $\mathcal{R} = 4$ cases with tip-panel actuation for the step-up and step-down gusts with acceleration or deceleration occurring over $1c$ of travel. For both gusts, actuation starts at $21.5c$ traveled. These were chosen as representative of the whole measurement set. The gray band in each plot shows the precision-error bounds; and note that for the mean C_L, the overline is omitted and implied from this point forward and in all plots. Also, in computing C_L, the instantaneous translational velocity of the main wing U_{main} and the time-varying wing area are employed. The precision error is overall lowest in the initial $Re = 18{,}000$ portion of the step-down gust, and it is highest after the step down to $Re = 9000$, where the data have more variation and the signal is smallest (Fig. 3b). For the cases shown in Fig. 3, the time average of the precision error in the mean C_L over the full motion duration is within ±4% (±0.05) and ±6.7% (±0.08) for the step-up and step-down gusts, respectively.

C. Experimental Parameters

The main rectangular wing is oriented vertically through the reasonably clean free surface, which acts as a reflected (symmetry) boundary condition if the free surface is flat [21,28]. For the rectangular wing with the tip panel fully retracted, the physically submerged aspect ratio is $\mathcal{R} = b/c$, which is set by varying the water level, where b is the wing span. Submerged $\mathcal{R} = 1$ and 2, which can approximately be doubled [21,28] to 2 and 4 by the reflection, are used for the rectangular-wing portion. In this study, the Froude number, $Fr = U/\sqrt{gd}$ (where g is the gravitational acceleration) is kept low (below 0.25, for a reference length d based on both the chord and submerged span for the cases tested) because for a Fr as high as 1, the free-surface wave effect dominates and causes suppression of the vortex shedding [29]. The free-surface deformations from wave effects, which were maximum during the gusts, are less than 2–3 mm. In our cases, when a prominent LEV forms and sheds, we see a clear depression of the free surface due to the low-pressure zone at the vortex core indicating that the vortex connects to the free surface normally. In this way, the free surface acts as a reflected boundary condition. However, due to the curvature on the free surface created in this process, some streamwise vorticity is generated [30]. This does not produce an "ideal" symmetry condition at the free-surface boundary; however, it is a good assumption. The vortex depression at the free surface is less than 0.5 cm (6% of the smallest submerged span considered here, i.e., $1c$). In Fig. 4a, we compare C_L data for fully submerged horizontal wings [5] (AFRL/UMD cases; AFRL/UMD is used in short for Air Force Research Lab/University

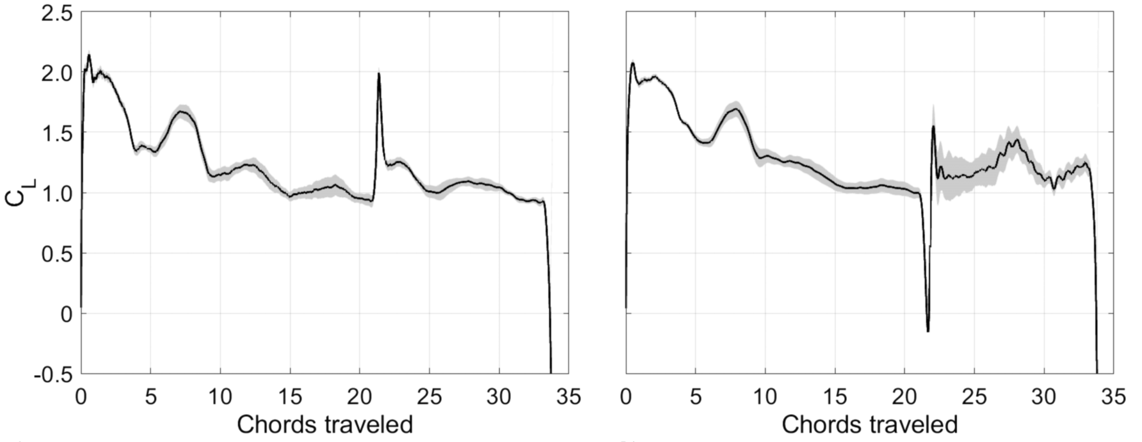

a) b)

Fig. 3 C_L **with the precision-error band (gray) for the** $AR = 4$ **rectangular wing; tip actuation at 21.5**c **traveled during a) step-up (actuation-in) and b) step-down (actuation-out) 1**c **gusts.**

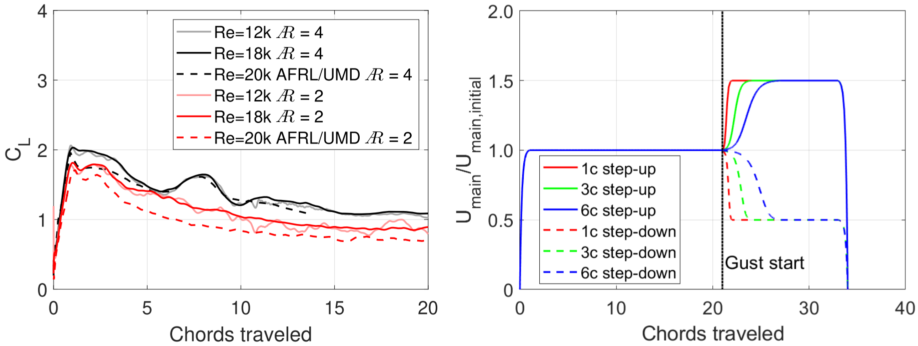

a) b)

Fig. 4 Plots of a) C_L **comparison between fully submerged horizontal and free-surface-piercing vertical wings for** $AR = 4$ **and 2; and b) main-wing motion profiles for the step-up and step-down gusts; k in the legend denotes thousands.**

of Maryland) with those of our vertical free-surface piercing wing, using their motion profiles. The $AR = 2$ case shows some deviation, whereas the $AR = 4$ data overlap very well. The discrepancy for $AR = 2$ is of a similar order to the C_L variations from different experimental setups and numerical simulations shown in Ref. [5] for $AR = 4$. Therefore, the free-surface effect is considered negligible for the parameters used here.

The translational motions of the main wing are simplified streamwise gustlike profiles. Similar to Mulleners et al. [26] and Marzanek and Rival [27], we examine step-up gusts, but also step-down gusts. They can be thought of as emulating headwind and tailwind gusts, respectively. Figure 4 shows the dimensionless wing velocity profiles versus chords traveled, nondimensionalized by the constant velocity just after the startup acceleration $U_{\text{main,initial}}$. The gust cases all begin with acceleration from rest over $1c$ to constant $U_{\text{main,initial}}$. At $21c$ traveled, the wing executes an additional acceleration to a higher constant velocity of $1.5U_{\text{main,initial}}$ for step-up gusts or deceleration to $0.5U_{\text{main,initial}}$ for step-down gusts. Therefore, the gust amplitude is 50% in each case, as for the step-up gusts of Mulleners et al. [26] and Marzanek and Rival [27]. Hyperbolic-tangent velocity profiles are used during all the acceleration and deceleration portions of the motions until the desired constant velocity is reached; these smooth profiles aid in mitigating mechanical vibrations. The hyperbolic-tangent curve is scaled to have the same average acceleration and duration as a constant-acceleration (linear) profile. The gusts are initiated after $20c$, and so startup effects are not prominent since the C_L approximately levels off to a low value and the wing exhibits more periodic LEV and TEV shedding (based on prior flow visualization by Chowdhury et al. [31]). Similar to the step-up study of Marzanek and Rival [27], acceleration/deceleration or "ramp" distances of $1c$, $3c$, and $6c$ before the wing reaches the final step-up/step-down velocity, respectively, are tested. After $12c$ of travel beyond the gust start, the wing decelerates and stops at a distance of $34c$.

The main-wing Reynolds number ($Re = U_{\text{main}}c/\nu$), where ν is the kinematic viscosity, is 12,000/18,000 and 18,000/9000 before/after the gust for the step-up and step-down cases, respectively. This is appropriate for small UAVs [32], and it yields sufficiently high signals from the force sensor. The C_L at $Re = 12{,}000$, which exhibits minimal free-surface deformations, matches that at the maximum $Re = 18{,}000$ tested within the error (Fig. 4a), for which the free-surface disturbances are somewhat larger, particularly in the vortex cores, but are otherwise small compared to the wing span. This indicates that adverse free-surface effects are not substantial over the Re range tested. The Re effects on C_L in this range have been shown to be minimal [33] and are not the focus of the present study. The angle of attack of the main wing is $\alpha = 45$ deg, which is chosen to produce flow separation with strong vortices, and due to the substantial prior work at this value. For $\alpha = 45$ deg, $AR = 4$, with the tip panel extended, the blockage ratio (submerged frontal-projected wing area divided by the filled tank cross-sectional area) is only ~1%.

The goal of this paper is to examine whether the tip-panel actuation can mitigate the lift change produced by the step-up/step-down gusts. However, as indicated in Sec. I, the aim here is to understand the panel's effect and not to do flow control or lift optimization. Inward rotation ("actuation-in") is employed to reduce the lift after the step-up gust, whereas outward rotation ("actuation-out") is used to increase the lift for the step-down case. For the former, the starting and ending values of Λ are 45 and 90 deg, whereas these are swapped for the latter. Chowdhury et al. [31] showed that actuation timing can substantially affect the flow structures, and here it is varied to study its influence on the lift. For all $1c$–$6c$ step-up/step-down gusts, two actuation timings are tested: 1) early actuation at $21.5c$ of travel, i.e., shortly after the gust initiation at $21c$; and 2) actuation at 50% of the travel distance during the ramp, namely, at $21.5c$, $22.5c$, and $24c$ traversed for the $1c$, $3c$, and $6c$ ramp, respectively (for the $1c$ ramp, the two timings are the same). The AR and wing area vary for each actuation type. With the panel retracted ($\Lambda = 90$ deg), the ARs are simply those for the rectangular cases, i.e., 2 and 4. For the fully extended tip panel with $\Lambda = 45$ deg, the AR increases to 4.1 and 6, respectively, with corresponding increases in wing area of 31.7% and 15.8%. As mentioned earlier, two reference cases with the same U_{main} profiles but fixed tip geometries are tested for comparison: 1) the rectangular case with the tip panel fully retracted (final geometry for actuation-in), and 2) the static-sweep case where the tip panel is extended to $\Lambda = 45$ deg (final geometry for actuation-out). Table 1 summarizes the motion cases.

The tip-panel motion is in addition to U_{main}, and it is characterized using the advance ratio, J. For flapping wings in forward flight [34], typically J is taken as the forward velocity component along the azimuthal (rotational) wingtip velocity divided by its absolute average value (excluding the superimposed translational velocity). The present tip panel has a tilted $\alpha = 45$ deg rotational stroke plane. Therefore, the component of the forward velocity in the plane of rotation $U_{\mathrm{main}} \cos\alpha$ is used similar to the definition for helicopters with a tilted rotor plane [35]. Since the tip panel has a sweep angle Λ, a factor of $\cos\Lambda$ is used to obtain the component of $U_{\mathrm{main}} \cos\alpha$ orthogonal to the panel LE. The final expression is $J = U_{\mathrm{main}} \cos\alpha \cos\Lambda / U_{\mathrm{panel,tip}}$, where $U_{\mathrm{panel,tip}}$ is the maximum, constant azimuthal tip velocity. For all cases, the tip-panel motion profile is trapezoidal with constant acceleration and deceleration occurring over the first and last 10% of the duration, respectively, having constant $U_{\mathrm{panel,tip}}$ in between; the rotational amplitude is always 45 deg giving $\Lambda = 45$ deg for maximum J. The constant-velocity magnitude for all cases, whether inward or outward panel rotation, is $U_{\mathrm{panel,tip}} = 1.5U_{\mathrm{main,initial}}$, with angular velocities of 3.05 rad/s for a pre-gust $Re = 12{,}000$ (step-up cases with actuation-in) and 4.58 rad/s for $Re = 18{,}000$ (step-down gusts having actuation-out). The actuation-in lasts for ~0.7 chords traveled by the main wing in the 50% actuation cases, and ~$0.5c$ traversed for $21.5c$ actuation in the $3c$ and $6c$ ramps. These values are ~$0.35c$ and ~$0.46c$, respectively, for actuation-out. The U_{main} changes during wing acceleration/deceleration for step-up/step-down gusts, with the largest value being for the 50% step-up profiles that yields a maximum $J = 0.5$ across all cases. For outward panel rotation, from extrapolation of the results of Harbig et al. [8] (cf. their figure 19) for the present $\mathit{AR} \approx 1$ tip panel, $J \leq 0.5$ should produce an attached LEV (here, swept-edge vortex or SEV). Harbig et al. [8] and Lentink and Dickinson [6] also describe the role of Ro for a rotating wing in forward motion, concluding that if the Ro is small (i.e., for short radial distances), LEV attachment can occur for low J. The tip panel's small AR should also have a sufficiently low Ro for SEV attachment, which our earlier flow visualization showed for starting flows [31].

III. Results

In the first part of this section, the results from the force measurements are presented for the rectangular reference case to show the key features of the step-up and step-down gust motions. Next, the actuation cases for $\mathit{AR} = 2$ and 4 are discussed. Note that the following analysis is based on a single tip-to-initial-main-wing velocity ratio of 1.5. Finally, we examine if superposition of the separate contributions from the actuation and gust predicts the actuation effect in a gust.

A. Rectangular Wing

Figure 5a gives the dimensional lift force L acting on the $\mathit{AR} = 4$ rectangular wing for step-up and step-down gust cases to show its behavior before calculating C_L. For step-up motions, the pre-gust Re is 12,000 and post-gust is 18,000; whereas for step-down, the Re drops from 18,000 to 9000: higher Re flow produces greater L. For the starting-flow portion with acceleration from rest over $1c$, all curves exhibit an initial peak due to fluid-inertial (added-mass) force and circulatory force from the vortex growth. This is followed by a second peak from vortex formation and shedding, and then a third, lower peak corresponding to another formation and shedding cycle. Mulleners et al. [26] describe the interactions with the prior flow structures that cause this last, prominent circulatory peak to be reduced. This behavior is similar to that of the fully submerged $\mathit{AR} = 4$ starting-flow cases from the NATO AVT-202 study, as reported by Stevens et al. [5]. Consistent with the 50% step-up gust

Table 1 Cases tested for the step-up/step-down gust motions for $\mathit{AR} = 2$ and 4; the Reynolds numbers are given in the text

Gust acceleration/deceleration distance	Tip conditions tested
	50% step-up gust at $21c$ traveled
$1c$	Rectangular, static sweep ($\Lambda = 45$ deg), actuation-in at $21.5c$
$3c$	Rectangular, static sweep ($\Lambda = 45$ deg), actuation-in at $21.5c$ and $22.5c$
$6c$	Rectangular, static sweep ($\Lambda = 45$ deg), actuation-in at $21.5c$ and $24.0c$
	50% step-down gust at $21c$ traveled
$1c$	Rectangular, static sweep ($\Lambda = 45$ deg), actuation-out at $21.5c$
$3c$	Rectangular, static sweep ($\Lambda = 45$ deg), actuation-out at $21.5c$ and $22.5c$
$6c$	Rectangular, static sweep ($\Lambda = 45$ deg), actuation-out at $21.5c$ and $24.0c$

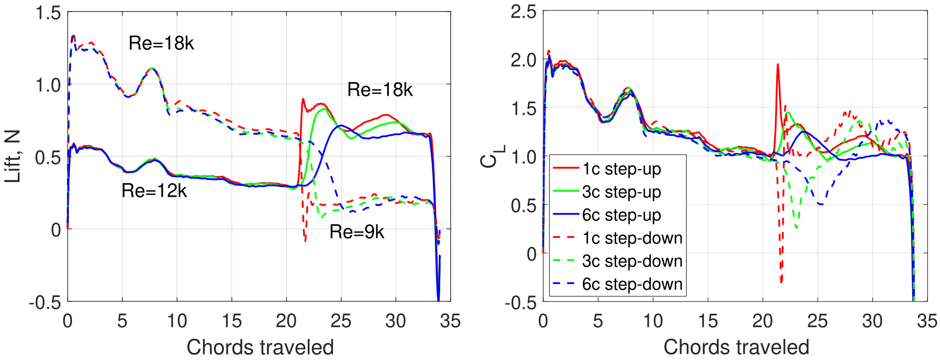

a) b)

Fig. 5 Force measurements for the $\mathit{AR} = 4$ rectangular wing with step-up and step-down gusts starting at $21c$ traveled: a) lift and b) C_L incorporating the instantaneous main-wing velocity.

study of Mulleners et al. [26], here, the qualitative lift trends for the $1c$-acceleration starting flow and $1c$ step-up gust resemble one another.

Figure 5b shows the corresponding $C_L = 2L/(\rho U_{\mathrm{main}}^2 S)$ plot, where ρ is the fluid density and S is the wing area. We use the time-varying U_{main} to scale the lift so that the C_L features can be attributed to unsteady-flow phenomena only. For the initial $1c$ startup acceleration, the C_L is instead nondimensionalized using $U_{\mathrm{main,initial}}$, since starting-flow scaling is not the focus of this paper. The C_L curves for $Re = 12{,}000$ and 18,000 before the gust collapse very well, as expected, given the Re independence mentioned earlier in this paper. Furthermore, Fig. 5b indicates that using the instantaneous U_{main} for C_L makes the pre- and post-gust values more comparable. Considering the $1c$ step-down case (red dashed curve), just after the gust, there is a negative force minimum from the added-mass contribution followed by a brief positive peak; the C_L scaling increases their relative magnitudes versus the dimensional lift. The positive peak perhaps denotes rapid recovery, but it is exaggerated by the mechanical backlash (see Fig. 5a). Similar sharp recovery is also observed for the $\mathcal{AR} = 2$ slower ramps in Fig. 8, but it is unaffected by vibration; further details are in the next subsection.

Figures 6a and 6b focus on the gust forces for the rectangular step-up and step-down cases. For the step-up gust, the $1c$ acceleration ramp yields a sharp initial peak with contributions from both added mass and circulatory force, followed by two progressively lower and broader circulatory-lift peaks (Fig. 6a). For the $3c$ ramp, the added-mass and initial circulatory-lift peaks combine into a single peak followed by a second, lower circulatory-force maximum. The $6c$ step-up gust also generates a single, broad first peak with the same contributions as that for the $3c$ ramp, but there is only a very weak second circulatory-force maximum that lies within the experimental error. For the step-down gust, the $1c$-ramp case exhibits a $C_L < 0$ peak during maximum deceleration; and each of the $3c$ and $6c$ ramps shows a clear C_L minimum, but with $C_L > 0$, corresponding to their maximum deceleration (Fig. 6b); the magnitudes of these minima are progressively smaller with greater deceleration distance. For the step-down gusts, after the C_L minima as the deceleration gives way to the slower constant-velocity motion, the $3c$ and $6c$ cases show a C_L recovery (increase) to a positive circulatory-force maximum. The $1c$ gust has a C_L plateau after the brief positive recovery/backlash peak, followed by a circulatory peak similar to the slower gust ramps.

For Figs. 6c and 6d, the chords traveled for the $3c$ and $6c$ gusts are shifted backward by half the gust width, i.e., $1.5c$ and $3c$, respectively, for both the step-up and step-down types. This shift yields an improved collapse of the step-up gust cases in terms of the timing of the first peaks for all gust ramps, as well as for the second circulatory peaks of the $1c$ and $3c$ gusts (Fig. 6c). For the step-down gusts, the shift brings the C_L minima closer in terms of chords traveled as expected (Fig. 6d). However, they do not line up perfectly because the greatest deceleration does not occur exactly at 50% in terms of chords traversed, but rather at 50% of the total deceleration duration in time. The circulatory C_L peaks that occur approximately at a 6-chord distance from the gust minima show a much better collapse via the shift, and the magnitudes are similar. These peaks are higher than the second circulatory peaks at the corresponding chords traveled for the step-up gusts, as well as the first step-up circulatory peaks as described here. In Fig. 6c, the first circulatory peaks for the $3c$ and $6c$ step-up gusts are masked by the contribution from added mass. The step-down circulatory peak for $6c$ is still higher than this resultant first step-up peak, and therefore is also higher than the circulatory peak for the same step-up ramp. For $3c$, the comparison is not initially obvious. Since the LEV circulation is proportional to the instantaneous wing velocity [36], the first step-up circulatory peak, having its main contribution from the time derivative of the LEV circulation [33], scales with the wing acceleration. Therefore, this $3c$ circulatory peak should be lower than that of the $1c$ ramp, making this peak value smaller than that of the step-down recovery peak. How a favorable reorganization of the vortices after wake impingement enhances the step-down C_L will be analyzed from flow visualization in a future study.

B. Tip-Panel Actuation and Aspect-Ratio Effects

Here, we examine the unsteady C_L behavior from the tip-panel actuation during the gusts, and we focus on the absolute changes with respect to the reference cases. Figure 7 shows the step-up gust cases

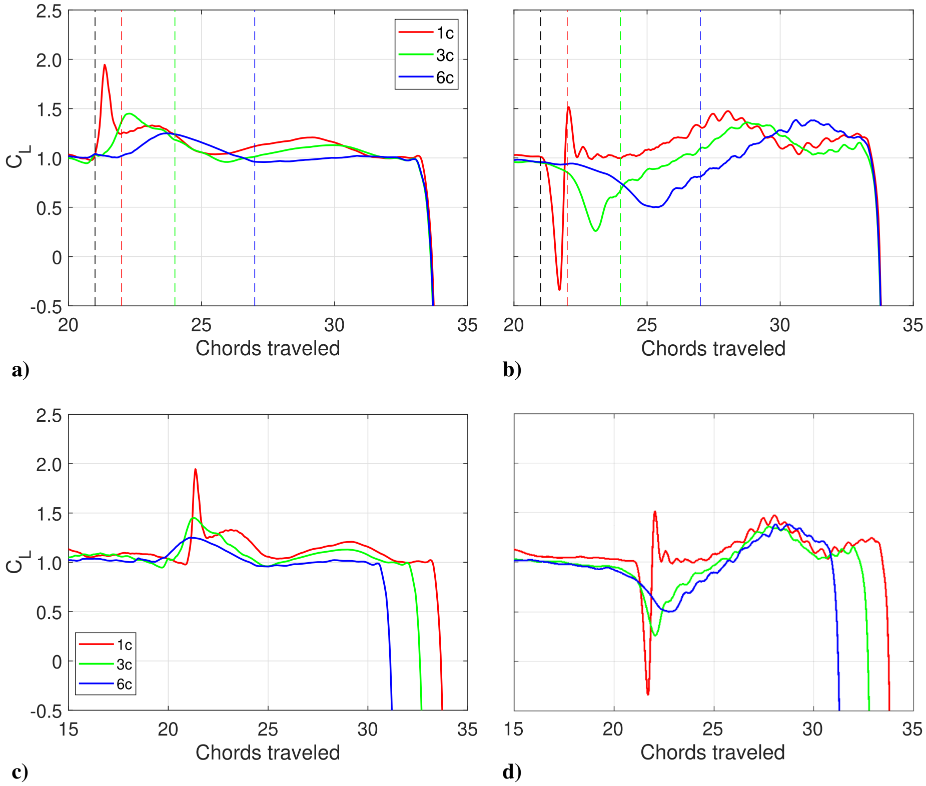

a) b) c) d)

Fig. 6 Lift coefficients for $\mathcal{AR} = 4$ rectangular wing in a,c) step-up and b,d) step-down gusts. $3c$ and $6c$ cases shifted backward by half the gust-acceleration distance in Figs. 6c and 6d.

including tip-panel actuation-in, and it compares data for $AR = 4$ (top row) and 2 (bottom row); recall that the AR refers to the rectangular portion of the wing. Per Sec. II.C, actuation occurring at $21.5c$ is tested for all acceleration/deceleration gust ramps, as well as 50% actuation which is done at the midpoint of the gust in terms of chords traveled. The 50% actuation happens at $21.5c$, $22.5c$, and $24c$ traveled for the $1c$, $3c$, and $6c$ gusts, respectively. For the tip-panel actuation cases, the C_L versus time incorporates both the instantaneous U_{main} for the velocity scale and the time-varying wing area. This again ensures that any deviations from the rectangular and static-sweep reference cases can be attributed to unsteady-flow phenomena.

For the step-up gusts with actuation-in (Fig. 7), the wing starts in the static-sweep condition; then, after actuation, the tip panel is fully retracted to the rectangular-wing case. Considering $AR = 4$, for the $1c$ ramp, actuation-in at $21.5c$ (50% actuation) occurs too late to affect the added-mass dominated initial peak, but it appreciably reduces both circulatory peaks afterward as compared to the static reference cases. A lower C_L from actuation versus the rectangular case indicates a truly unsteady-flow effect that cannot be accounted for by the difference in static geometry of the rectangular and static-sweep cases. The flow visualization results of Chowdhury et al. [31] indicate that a key contributor to this C_L reduction is likely the shedding of the panel SEV–TV–TEV loop as the panel quickly retracts into the wing. Note that in between the circulatory peaks (~$25.5c$ traveled), presumably after the main-wing vortex system sheds, the C_L for all $1c$-ramp cases is nearly the same. The overall C_L-reduction effect from inward actuation lasts for the remainder of the measurement, at least $12.5c$ traveled beyond the gust. The 50% actuation-in for the $3c$ ramp also does not affect the first C_L peak magnitude; but just after this, the actuation lowers the C_L below that of the reference cases for the rest of the motion, except again near the local minimum where shedding occurs. For the $6c$ gust, the 50% actuation timing also reduces the C_L between the first peak and shedding, although the effect is small; after which, the actuation-in case is similar to the reference geometries, except for a slight C_L decrease again near the end of the motion. The $21.5c$ actuation-in for the $3c$ ramp reduces the peak C_L during the gust; but afterward, the C_L nearly matches the reference cases. For the $6c$-ramp and $21.5c$ actuation, the C_L curve is slightly below those of the reference wings in the first part of the peak. Overall, the 50% actuation timing has the greatest and most sustained C_L-reduction effect, being most pronounced post-gust for the $1c$ ramp. However, it is too late to influence the entire gust peak for the $1c$ ramp and the rising portions of the $3c$ and $6c$ peaks.

The corresponding $AR = 2$ step-up gust cases are shown in the second row of Fig. 7. Compared to $AR = 4$, the C_L curves for $AR = 2$ have an overall lower magnitude, which is consistent with the smaller AR. For the $1c$ and $3c$ ramps, for $AR = 2$, a second circulatory-force peak is not present in almost all cases, except where a slight maximum exists for the static-sweep geometry; whereas this feature is prominent for $AR = 4$. Considering that the step-up gust shows similarities with starting flows, this is consistent with the starting-flow AR trends from Stevens et al. [5] and Taira and Colonius [3]. The latter study showed less-pronounced C_L peaks from vortex shedding for $AR = 2$ versus 4 at $\alpha = 40$ deg due to the greater effect of downwash from the wingtip vortices.

Overall, actuation-in for $AR = 2$ produces a larger change in C_L magnitude (with respect to the reference cases) during and shortly after the gust compared to $AR = 4$, which is expected given that the extended $AR = 2$ tip panel has a relatively greater percentage of the total wing area. This AR difference is evident during the first circulatory peak for the $1c$ ramp and the initial gust peaks for the $3c$ and $6c$ cases. This change is related to a dynamic flow effect, since the variable wing area is accounted for in C_L. However, for $AR = 2$, the panel's actuation effect is less sustained for the $1c$ case, and particularly for the $3c$ and $6c$ ramps, versus $AR = 4$; the actuation influence is negligible after $25c$ and $27c$ of travel for the $3c$ and $6c$ ramps, respectively. This may be related to the lack of a prominent, second circulatory force peak for $AR = 2$; whereas for $AR = 4$, the moving panel has a stronger second LEV to interact with [3], yielding an improved C_L reduction. Therefore, in general, the tip-panel actuation-in is more effective in reducing C_L peaks when there is a stronger inboard LEV forming and shedding; further quantitative flow information is needed to explore this.

Figure 8 gives the actuation-out cases for the step-down gusts. The wing begins with the rectangular geometry; then the tip panel rotates outward to have the static-sweep planform. For $AR = 4$ (top row), overall, the actuation increases the C_L compared to the reference cases both during and after the gust, depending on the ramp length. For the $1c$ ramp, the magnitude of the negative C_L peak is reduced substantially and the post-gust C_L plateau is higher than the reference cases. The flow visualization of Chowdhury et al. [31], albeit for a starting flow, shows an SEV forming on the outward rotating panel

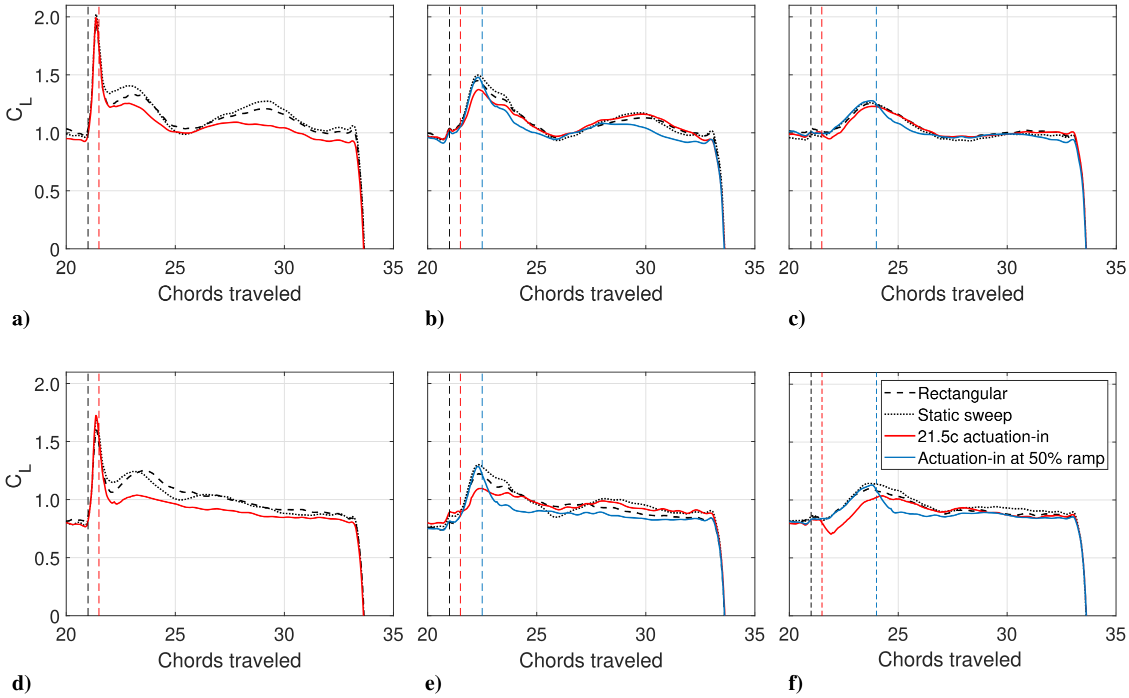

Fig. 7 **Results for the step-up gust with tip-panel actuation-in: a,d) $1c$ ramp; b,e) $3c$ ramp, and c,f) $6c$ ramp. $AR = 4$ (top row) and $AR = 2$ (bottom row).**

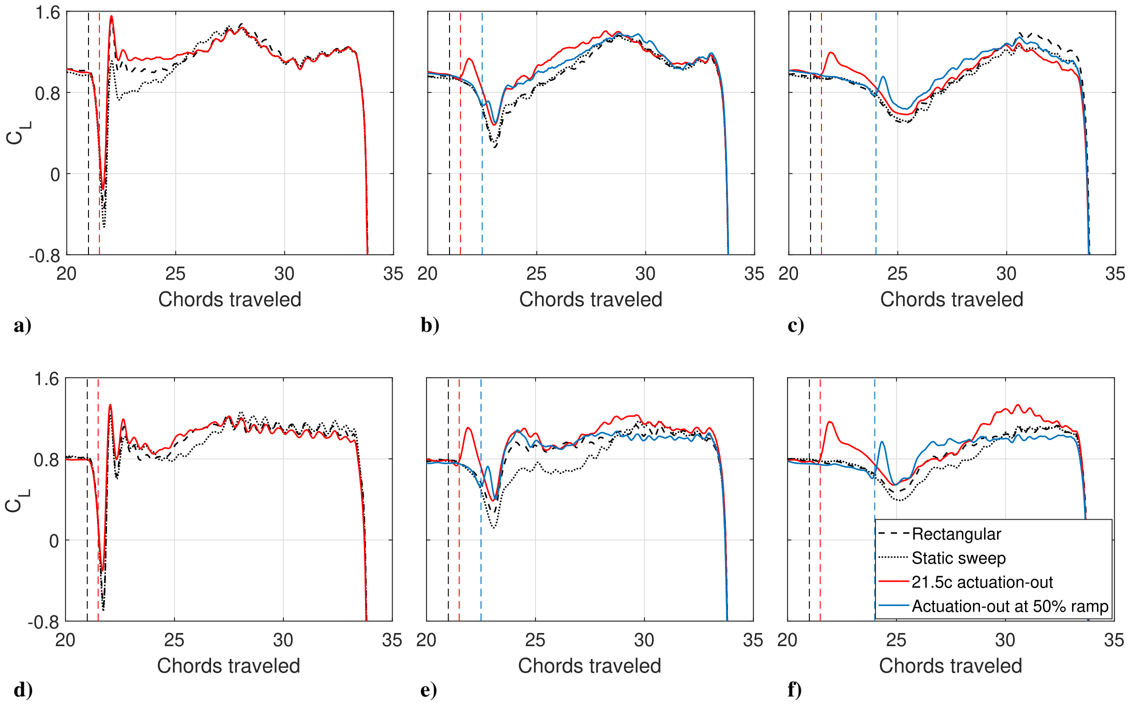

Fig. 8 **Results for the step-down gust with tip-panel actuation-out: a,d) 1*c* ramp; b,e) 3*c* ramp, and c,f) 6*c* ramp. $AR = 4$ (top row) and $AR = 2$ (bottom row).**

and an increase in the TEV/TV vortex loop size. If similar flow structures are present for the gust case, these features would contribute to this enhanced C_L. For the $3c$ ramp, the $21.5c$ actuation-out produces a high C_L peak; then the C_L lowers but maintains a larger value than the references cases until the first circulatory recovery peak at ~$28.5c$ traveled. The 50% actuation-out at $22.5c$ traveled for the $3c$ ramp occurs just before the C_L minimum from the gust. At first, it yields a C_L similar to the $21.5c$ actuation case, but then the C_L is reduced and gradually converges to essentially match the reference cases just before the recovery peak.

Considering the $6c$ ramps, for $21.5c$ actuation-out, the C_L overshoots the reference cases initially; then after $2c$ of further travel, the C_L becomes very close to the reference results, within the error. For 50% actuation-out at $24c$ traversed, there is again an overshooting C_L peak, and the C_L during the gust minimum is somewhat higher than that of the fixed-geometry reference cases, including the $21.5c$ actuation result. The C_L continues to be slightly above all other cases until the recovery peak. In the case of the $21.5c$ actuation, the improvement persists for a shorter duration than the 50% actuation case because the $21.5c$ actuation occurs perhaps too early before the gust minimum. In summary, for the $AR = 4$ step-down gusts, actuation-out not long before the C_L gust minimum (here 50% actuation) can reduce the magnitude of the drop in lift; and the effect is sustained above the uncertainty until approximately the C_L recovery peak for $3c$ and $6c$ ramps, and the second circulatory peak for the $1c$ ramp, i.e. for about 4–5 chords traveled. This effect also occurs with $21.5c$ actuation for the $3c$ ramp. In addition, the $21.5c$ actuation case produces a higher actuation peak than the 50% timing, as well as for the $6c$ ramp.

The $AR = 2$ actuation-out results for the step-down gusts are shown in Fig. 8 (second row). Overall, the rectangular and static-sweep reference cases show larger differences from one another compared to $AR = 4$, with the static-sweep wing exhibiting reduced C_L for certain durations after the gust start depending on the ramp length, but eventually the two cases merge. This is likely due to the relatively greater change in the swept portion of the wing and AR between the rectangular and static-sweep cases versus $AR = 4$; but without flow data, the exact cause is unknown. The C_L behavior for the actuation cases is very similar to that of the rectangular wing after the gust minimum, except for some deviations: for the $3c$ gust, the $21.5c$ actuation C_L has a small peak above the rectangular curve at about $29c$ traveled; and for the $6c$ gust, the $21.5c$ and 50% actuation cases have higher C_L at approximately $30c$ and $27c$ traveled, respectively. Note that the rectangular planform is what the actuation case starts with, with the static sweep being the final geometry; currently, the reasons for the closer comparison between the actuation and rectangular cases are unknown. For the $AR = 2$, $1c$ ramp, the actuation-out at $21.5c$ reduces the magnitude of the $C_L < 0$ gust peak and then recovers to a positive circulatory peak as with $AR = 4$; the recovery peak is contaminated by mechanical vibration, showing two peaks in Fig. 8d. After this recovery peak, the static-sweep case drops below the other curves until all C_L curves converge at about $27.5c$ traveled and remain overlapped through the end of the motion. This converging behavior also occurs for $AR = 4$ but earlier; however, for $AR = 2$, afterward the C_L levels off until the final wing deceleration. A post-recovery plateau starting at similar chords traveled is also observed for 50% actuation-out in the $3c$ and $6c$ gusts, lasting until the deceleration of the wing, perhaps because of a lack of strong LEV shedding; future flow analysis will help identify the cause.

For both the $3c$ and $6c$ ramps, the $21.5c$ and 50% actuation-out curves exhibit overshooting C_L peaks above the reference cases before the gust minimum, which are larger in magnitude than the corresponding $AR = 4$ actuations. These actuation timings do not substantially reduce the magnitude of the gust minimum. For the $3c$ ramp, the C_L increases after the minimum with a higher slope compared to the corresponding $AR = 4$ cases; the C_L for static-sweep still falls below the rectangular case, unlike $AR = 4$. The $AR = 2$, $6c$ ramp shows C_L recovery peaks at an earlier chords traveled for 50% actuation-out, and at a similar instant for the $21.5c$ actuation case with respect to $AR = 4$. The relative distance between the recovery peak of the 50% actuation cases and gust minimum is comparable for all three ramps of $AR = 2$. The $21.5c$ actuation C_L curves have maxima approximately $6c$ after the gust minimum like all $AR = 4$ cases; the static sweep shows a similar behavior. This is perhaps related to the higher AR (from $AR = 2$ to 4.1) achieved near the beginning of the gust.

For the step-down gusts, a summary comparison of the actuation-out effect between $AR = 4$ and 2 is somewhat confounded by differences in the C_L behavior of the rectangular and static-sweep reference cases for each AR. These aside, the tip-panel actuation-out for both ARs yields significant reductions of the C_L drop from the step-down gust, which is beneficial for gust mitigation (see Sec. III.D for the percentage of gust-impulse mitigation). For the two longer gust ramps, the $\mathit{AR} = 2$ actuation cases have relatively larger peaks just after actuation, versus the reference geometries, compared to $\mathit{AR} = 4$. Furthermore, for $\mathit{AR} = 2$, the rectangular and actuation cases allow for a faster post-gust recovery (C_L increase) for the $3c$ ramps, and 50% actuation produces a similarly earlier recovery for the $6c$ ramp, which is not found for $\mathit{AR} = 4$.

C. Effect of Actuation in the No-Gust Condition

Here, we present the effects of tip-panel actuation for the no-gust condition at various distances traveled by the main wing. Furthermore, we test how well superposition of the C_L from actuation with no gust onto that for no actuation with a gust predicts the real actuation effects during a gust. Figure 9 shows actuation-out early in the main-wing translation for $\mathit{AR} = 2$ and 4, at distances traveled of $1.5c$, $5.8c$, and $8c$, with no gust motion. Studying the actuation effects in the starting flow is useful in understanding how the effects change for the quasi-steady flow, which will be discussed later. There are clear differences in effectiveness based on how the tip-panel actuation is timed with a given vortex formation and shedding cycle (C_L maximum followed by minimum, respectively), particularly for $\mathit{AR} = 4$, where these features are more prominent. Only for $\mathit{AR} = 4$ and actuation-out at the $8c$ distance, which coincides with the second circulatory peak (i.e., right before the LEV shedding starts for that cycle) is there a sustained C_L increase in addition to the added-mass peak due to actuation; the effect lasts for $\sim 7c$ of wing travel (Fig. 9a). If the actuation-out occurs during the vortex-growth portion (C_L rise) of a formation/shedding cycle, such as at $1.5c$ traveled in the first cycle and $5.8c$ during the second (Fig. 9a), after the added-mass peak from actuation, the C_L increase is very short-lived and then nearly zero with respect to the final geometry (static-sweep case). For $\mathit{AR} = 2$ a similar trend is observed: actuation-out at $1.5c$ (early in the first and only prominent formation/shedding event) produces an added-mass dominated peak, then the C_L difference diminishes as soon as the main-wing LEV sheds (Fig. 9b). The other two actuation timings, at $5.8c$ and $8c$ traveled, have similar C_L changes, because of the lack of prominent shedding for $\mathit{AR} = 2$.

Figure 10a shows the effect of actuation for two different timings later in the motion, when the C_L reaches a quasi-steady level (near where the gusts in the Secs. III.A and III.B cases are executed). Here, the effect of the panel actuation outward (solid black and solid gray curves) decreases for both ARs due to the lack of a coherent LEV on the wing for the panel to influence. This is also the reason for the negligible C_L change observed for the tip actuation inward (Fig. 10, solid red and light red curves). Therefore, the linear superposition of this negligible C_L change for the actuation-in no-gust cases onto the corresponding reference gusts is to no purpose, meaning the actuation-in effect in the presence of a gust (Fig. 7) is completely attributed to the nonlinearity of the flow change due to the moving-panel/gust interaction. Two actuation-out timings, $21.5c$ and $22.5c$, result in a similar C_L behavior for $\mathit{AR} = 4$ and 2, consisting of an added-mass dominated peak followed by a gradual decrease, with the $\mathit{AR} = 2$ changes being slightly higher, likely due to the larger panel area relative to that of the main wing.

The $21.5c$ and $22.5c$ actuation-out cases are used here for testing a superposition estimation for the $1c$ and $3c$ gust ramps. The C_L for the rectangular case (initial geometry) is subtracted from the C_L for the $21.5c$ and $22.5c$ actuation-out cases, respectively, each for the no-gust condition. These differences (moving tip-panel effect) are then added to the C_L for the rectangular wing for the $1c$- and $3c$-ramp step-down gusts (gust effect). Figure 11 shows the comparison between these superposed C_L and the corresponding actuation-out cases that occur during gusts. The superposition matches very well with the actuation-gust case for the $1c$ ramp for $\mathit{AR} = 2$ and 4, except for the recovery peak where the superposed C_L is higher than its

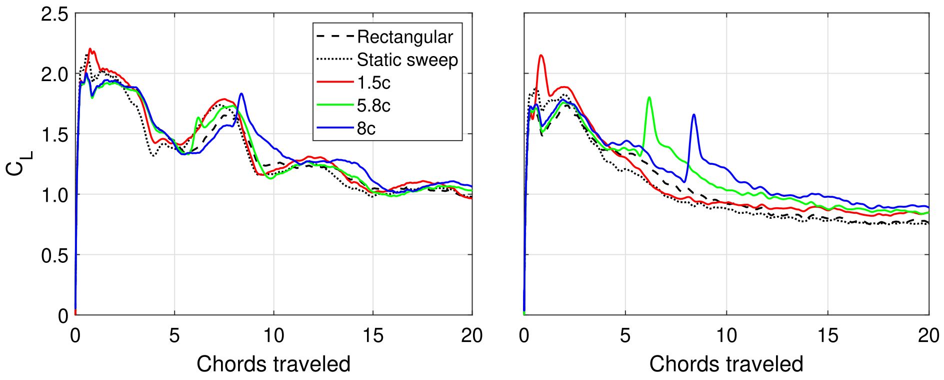

a) b)

Fig. 9 Results for actuation-out at $1.5c$, $5.8c$, and $8c$ in the starting flow for a) $\mathit{AR} = 4$ and b) $\mathit{AR} = 2$, with the rectangular and static-sweep cases.

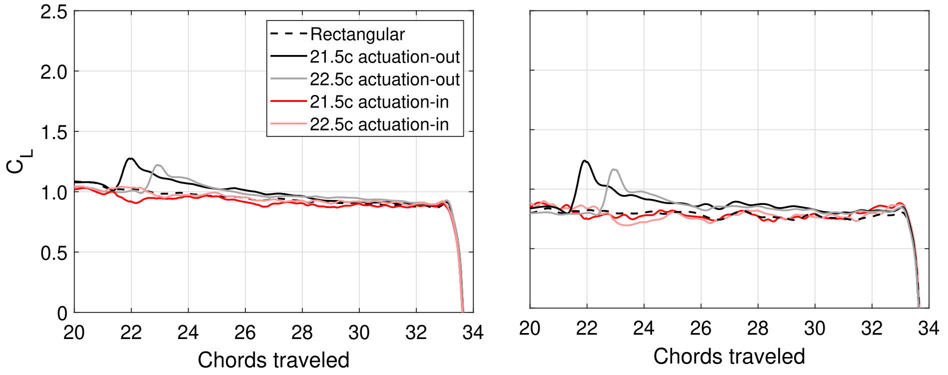

a) b)

Fig. 10 Results for the actuation-out and -in cases at $21.5c$ and $22.5c$ traveled without a gust for a) $\mathit{AR} = 4$ and b) $\mathit{AR} = 2$, versus the rectangular case.

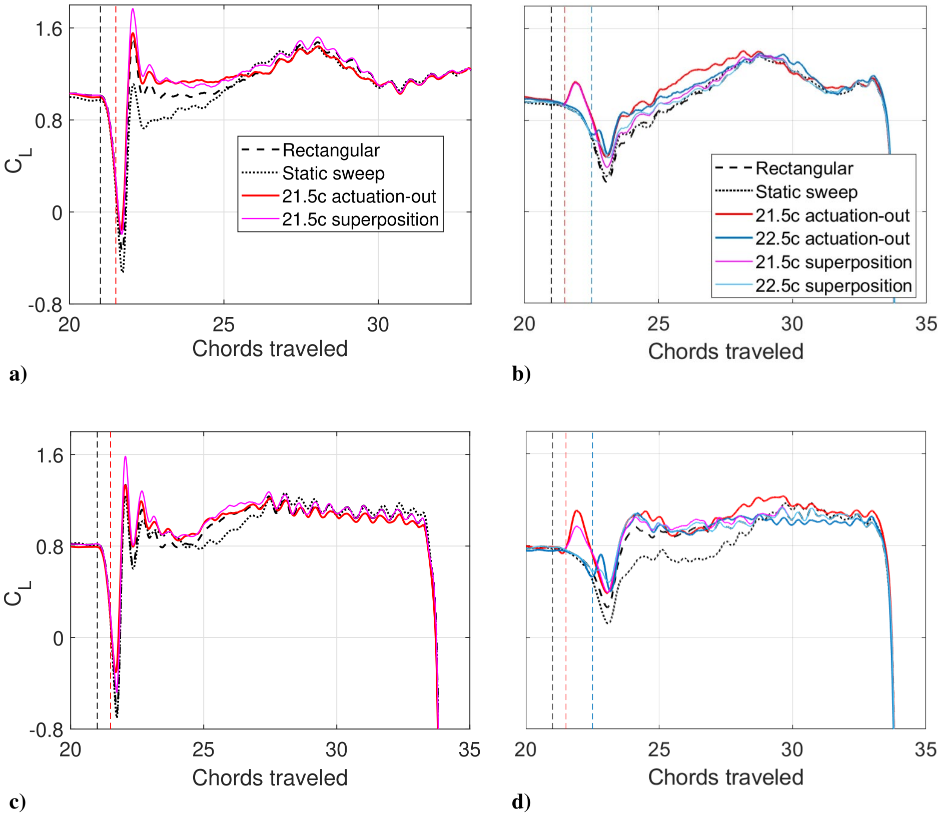

Fig. 11 Superposition comparison with the actuation-out cases during step-down gusts: a,c) 1*c* ramp and b,d) 3*c*-ramp; Æ = 4 (top row) and Æ = 2 (bottom row).

counterpart. This is expected since the shed vortex structures from the main wing due to the strong gust deceleration should adversely affect the formation of the new panel vortices. However, gust alleviation is greater in the gust minimum when the tip is actuated during the gust for Æ = 2.

For the 3c ramp, the superposition nearly matches or underpredicts the actual C_L. It underpredicts the initial peak for Æ = 2, 21.5*c* actuation and those for the 22.5*c* actuation: both Æs. Therefore, for Æ = 2, all the gust-actuation cases show better performance during the gust versus the superposition estimates. Also, it underpredicts the sustained post-gust C_L recovery, mainly for Æ = 4. These differences are the result of nonlinear interactions of the main-wing and moving-panel vortex structures. Despite these differences, during the gust interaction, the linear superposition works reasonably well for outward tip actuation. This is not the case for the wing with inward tip actuation; any gust alleviation is due to the complex interaction of the main-wing vortices and shed structures from the tip panel.

D. Gust-Impulse Change from Tip Actuation

As shown in Sec. III.B, the actuation effects during the gust are highly unsteady; therefore, comparing the effectiveness across cases is not straightforward. A simple impulse metric is used to characterize the gust alleviation performance: the percentage of the total impulse difference between the gust-actuation and -reference cases, with respect to the total impulse change between the gust and no-gust reference cases (no-gust C_L curves are shown in Fig. 10). The total impulse for the step-up gusts is calculated from the start of the gust (21*c*) until the final main-wing deceleration begins (33*c*). For the step-down gusts, the gust C_L first drops below the no-gust level; but, after the gust-deceleration stops, it recovers and continues to increase to a much higher value than the no-gust counterpart. The impulse calculation period is taken from 21*c* to the point when the reference case C_L crosses its no-gust level to only focus on the gust alleviation during the lift drop. The actuation-out is intended to boost the C_L, but the C_L increase after it recovers beyond the no-gust value is not required. The reference case for the calculation is the wing configuration that the actuation case starts with, i.e., static sweep for actuation-in and rectangular for actuation-out. The impulse is chosen as the metric versus the C_L, to account for both the force change and the duration of the effect. Note that in Sec. III.B, the comparisons were made based on C_L in the absolute sense; whereas here, they are in terms of impulse in the relative sense, relative to the no-gust situation.

Table 2 shows the percentage of gust alleviation for both Æs and each gust type with the three different ramps. For the step-up gust, actuation-in can reduce the impulse change from the gust by as much as 38% (6*c* ramp, 21.5*c* actuation, Æ = 2). The actuation-in

Table 2 Percentage of the gust-impulse reduction/recovery by the actuation-in/-out for a C_L increase/decrease due to the step-up/-down gust for Æ = 4 and 2

	Æ	1*c* ramp 21.5*c* actuation	3*c* ramp 21.5*c*/50% actuation	6*c* ramp 21.5*c*/50% actuation
Step-up gust	4	17	7/24	22/26
Actuation-in	2	34	33/22	38/33
Step-down gust	4	17	84/66	51/48
Actuation-out	2	59	65/52	74/64

performs better for the $\mathcal{R} = 2$ wing for all three gust ramps, as also found in the unsteady C_L analysis (Sec. III.B). The 50% actuation-in cases have greater gust-impulse mitigation than the 21.5c actuation-in for the 3c- and 6c-ramp cases for $\mathcal{R} = 4$, but this is opposite for $\mathcal{R} = 2$. Actuation-out can reduce the impulse drop in the step-down gust by almost 84% (3c ramp, 21.5c actuation, $\mathcal{R} = 4$). All 21.5c actuation-out cases achieve higher recovery than the 50% actuation cases. However, the 21.5c actuation-out is too early to significantly affect the unsteady C_L minimum but has a high actuation peak magnitude, and 50% actuation performs better around the gust-C_L minimum (Fig. 8b). This impulse study principally shows the potential of the tip-panel actuation for mitigating gusts. Further work is needed to optimize the C_L-change behavior in time. Overall, both actuation types show promising gust-mitigation performance.

IV. Conclusions

A tip panel with aft sweep was rotated inward or outward on a low-$\mathcal{R}$ $\alpha = 45$ deg rectangular main wing in translation to study its ability to mitigate lift variations from streamwise gusts of two kinds: step-up and step-down, respectively. Three gust ramps over distances traveled of 1c, 3c, and 6c with two actuation timings, near the gust start (21.5c traveled) and at 50% of the ramp distance, were tested for $\mathcal{R} = 4$ and 2, where the $\mathcal{R}$ values correspond to the rectangular-wing portion only. The actuation cases were compared to two fixed-geometry references: the rectangular (panel retracted) and static-sweep (panel extended) wings. The C_L definition used both the instantaneous main-wing translation velocity and the variable wing area. First, the gust study for the $\mathcal{R} = 4$ rectangular wing revealed interesting comparative features across the three ramps between the two kinds of gusts. The 1c step-up gust exhibits unsteady lift behavior similar to that of the 1c starting motion, as found by others. For step-down gusts, the deceleration produces a C_L minimum, and then the force recovers to a circulatory peak. For the 1c ramp, it recovers sharply right after the end of deceleration and forms a plateau leading to a circulatory peak, which aligns with the first recovery (circulatory) peaks for the 3c and 6c gusts when they are shifted back by the 50% ramp distance. For the step-up gust cases, there are two circulatory peaks, except for the 6c ramp, which has only the first. The post-gust circulatory peaks for the step-down gusts are higher than the step-up circulatory peaks.

For the panel actuation, a single tip-to-main-wing velocity ratio is used. In step-up gusts, the actuation-in reduces the force from the pre- and post-geometry cases in the circulatory peak regions; the reductions are greater for $\mathcal{R} = 2$. The most pronounced effect on the gust peak and post-gust C_L was observed for the 3c and 1c ramps, respectively. For both $\mathcal{R}$, actuation-in at the 50% ramp distance yields the most sustained reduction in C_L but does not affect the gust peak, whereas the early actuation at 21.5c for the 3c ramp (and the 6c ramp for $\mathcal{R} = 2$) lowers this peak magnitude. The step-down gusts show greater differences in C_L between the rectangular and static-sweep cases than the step-up gusts; the deviation is particularly larger for $\mathcal{R} = 2$. For $\mathcal{R} = 4$, the actuation-out increases the C_L compared to the reference cases both during and after the gust. The $\mathcal{R} = 2$ actuation-out generates relatively higher actuation peaks in C_L versus $\mathcal{R} = 4$. Combining the performance in C_L and duration, an impulse calculation shows the potential for gust mitigation of both types of actuation: the impulse change due to gusts can be reduced as much as 38% by actuation-in and 84% by actuation-out. However, flow data are needed to better understand the vortex dynamics underlying the wingtip-panel performance. In the future, optimization is required to maximize the actuation effects in terms of lift distribution with time.

A superposition of the no-gust-actuation result onto the gust C_L without actuation was compared with the actuation effects in the gust. The superposition matches reasonably well with the real actuation-out effects in the gust, except for a few deviations. However, the actuation-in effect is negligible in the no-gust condition. Therefore, the gust mitigation by actuation-in is purely a result of nonlinear vortex interactions.

Acknowledgments

This work is supported by the National Science Foundation, award no. CBET-1706453, supervised by Ronald Joslin. We would like to thank Cameron Smith, Karan Shah, and Samuel Slick for their assistance with the experimental setup and with acquiring some of the results. The authors appreciate the valuable feedback from the anonymous reviewers, which improved the paper's quality and clarity.

References

[1] McCroskey, W. J., "Unsteady Airfoils," *Annual Review of Fluid Mechanics*, Vol. 14, No. 1, 1982, pp. 285–311.
https://doi.org/10.1146/annurev.fl.14.010182.001441

[2] Dickinson, M. H., and Gotz, K. G., "Unsteady Aerodynamic Performance of Model Wings at Low Reynolds Numbers," *Journal of Experimental Biology*, Vol. 174, No. 1, 1993, pp. 45–64.

[3] Taira, K., and Colonius, T., "Three-Dimensional Flows Around Low-Aspect-Ratio Flat-Plate Wings at Low Reynolds Numbers," *Journal of Fluid Mechanics*, Vol. 623, March 2009, pp. 187–207.
https://doi.org/10.1017/S0022112008005314

[4] Jardin, T., Farcy, A., and David, L., "Three-Dimensional Effects in Hovering Flapping Flight," *Journal of Fluid Mechanics*, Vol. 702, May 2012, pp. 102–125.
https://doi.org/10.1017/jfm.2012.163

[5] Stevens, P. R. R. J., Babinsky, H., Manar, F., Mancini, P., Jones, A. R., Nakata, T., Phillips, N., Bomphrey, R. J., Gozukara, A. C., Granlund, K. O., and Ol, M. V., "Experiments and Computations on the Lift of Accelerating Flat Plates at Incidence," *AIAA Journal*, Vol. 55, No. 10, 2017, pp. 3255–3265.
https://doi.org/10.2514/1.J055323

[6] Lentink, D., and Dickinson, M. H., "Rotational Accelerations Stabilize Leading Edge Vortices on Revolving Fly Wings," *Journal of Experimental Biology*, Vol. 212, April 2009, pp. 2705–2719.
https://doi.org/10.1242/jeb.022269

[7] Jardin, T., and Colonius, T., "On the Lift-Optimal Aspect Ratio of a Revolving Wing at Low Reynolds Number," *Journal of the Royal Society, Interface*, Vol. 15, No. 143, June 2018, pp. 1–16.
https://doi.org/10.1098/rsif.2017.0933

[8] Harbig, R. R., Sheridan, J., and Thompson, M. C., "The Role of Advance Ratio and Aspect Ratio in Determining Leading-Edge Vortex Stability for Flapping Flight," *Journal of Fluid Mechanics*, Vol. 751, June 2014, pp. 71–105.
https://doi.org/10.1017/jfm.2014.262

[9] Jones, A. R., Pitt Ford, C. W., and Babinsky, H., "Three-Dimensional Effects on Sliding and Waving Wings," *Journal of Aircraft*, Vol. 48, No. 2, 2011, pp. 633–644.
https://doi.org/10.2514/1.C031184

[10] Hartloper, C., Kinzel, M., and Rival, D. E., "On the Competition Between Leading-Edge and Tip-Vortex Growth for a Pitching Plate," *Experiments in Fluids*, Vol. 54, No. 1447, 2013, Paper 1447.
https://doi.org/10.1007/s00348-012-1447-5

[11] Beem, H. R., Rival, D. E., and Triantafyllou, M. S., "On the Stabilization of Leading-Edge Vortices with Spanwise Flow," *Experiments in Fluids*, Vol. 52, No. 2, 2012, pp. 511–517.
https://doi.org/10.1007/s00348-011-1241-9

[12] Wong, J. G., Kriegseis, J., and Rival, D. E., "An Investigation Into Vortex Growth and Stabilization for Two-Dimensional Plunging and Flapping Plates with Varying Sweep," *Journal of Fluids and Structures*, Vol. 43, Nov. 2013, pp. 231–243.
https://doi.org/10.1016/j.jfluidstructs.2013.09.010

[13] Wong, J. G., and Rival, D. E., "Determining the Relative Stability of Leading-Edge Vortices on Nominally Two-Dimensional Flapping Profiles," *Journal of Fluid Mechanics*, Vol. 766, Feb. 2015, pp. 611–625.
https://doi.org/10.1017/jfm.2015.39

[14] Klaassen van Oorschot, B., Mistick, E. A., and Tobalske, B. W., "Aerodynamic Consequences of Wing Morphing During Emulated Take-Off and Gliding in Birds," *Journal of Experimental Biology*, Vol. 219, No. 19, 2016, pp. 3146–3154.
https://doi.org/10.1242/jeb.136721

[15] Nikolic, V. R., "Optimal Movable Wing Tip Strake," *Journal of Aircraft*, Vol. 48, No. 1, 2011, pp. 335–341.
https://doi.org/10.2514/1.c031014

[16] Lee, T., and Pereira, J., "Modification of Static-Wing Tip Vortex via a Slender Half-Delta Wing," *Journal of Fluids and Structures*, Vol. 43, Nov. 2013, pp. 1–14.
https://doi.org/10.1016/j.jfluidstructs.2013.08.004

[17] Reynolds, K. V., Thomas, A. L. R., and Taylor, G. K., "Wing Tucks are a Response to Atmospheric Turbulence in the Soaring Flight of the Steppe Eagle *Aquila nipalensis*," *Journal of the Royal Society, Interface*, Vol. 11, No. 101, Dec. 2014, pp. 1–11. https://doi.org/10.1098/rsif.2014.0645

[18] Wang, S., Zhang, X., He, G., and Liu, T., "Lift Enhancement by Bats? Dynamically Changing Wingspan," *Journal of the Royal Society, Interface*, Vol. 12, No. 113, 2015, pp. 1–11. https://doi.org/10.1098/rsif.2015.0821

[19] Chin, D. D., Matloff, L. Y., Stowers, A. K., Tucci, E. R., and Lentink, D., "Inspiration for Wing Design: How Forelimb Specialization Enables Active Flight in Modern Vertebrates," *Journal of the Royal Society, Interface*, Vol. 14, No. 131, 2017, pp. 1–18. https://doi.org/10.1098/rsif.2017.0240

[20] Joshi, K., Kauffman, J. L., Vazquez, C. G., and Bhattacharya, S., "Unsteady Maneuvering of a Morphing Wing," AIAA Paper 2020-0333, 2020. https://doi.org/10.2514/6.2020-0333

[21] Wibawa, M., Steele, S. C., Dahl, J. M., Rival, D. E., Weymouth, G. D., and Triantafyllou, M. S., "Global Vorticity Shedding for a Vanishing Wing," *Journal of Fluid Mechanics*, Vol. 695, Feb. 2012, pp. 112–134. https://doi.org/10.1017/jfm.2011.565

[22] Steele, S. C., Dahl, J. M., Weymouth, G. D., and Triantafyllou, M. S., "Shape of Retracting Foils that Model Morphing Bodies Controls Shed Energy and Wake Structure," *Journal of Fluid Mechanics*, Vol. 805, Sept. 2016, pp. 355–383. https://doi.org/10.1017/jfm.2016.553

[23] Di Luca, M., Mintchev, S., Heitz, G., Noca, F., and Floreano, D., "Bioinspired Morphing Wings for Extended Flight Envelope and Roll Control of Small Drones," *Interface Focus*, Vol. 7, No. 1, 2017, pp. 1–11. https://doi.org/10.1098/rsfs.2016.0092

[24] Hui, Z., Zhang, Y., and Chen, G., "Tip-Vortex Flow Characteristics Investigation of a Novel Bird-Like Morphing Discrete Wing Structure," *Physics of Fluids*, Vol. 32, March 2020, Paper 035112. https://doi.org/10.1063/1.5144432

[25] Granlund, K., Monnier, B., Ol, M., and Williams, D., "Airfoil Longitudinal Gust Response in Separated vs. Attached Flows," *Physics of Fluids*, Vol. 26, No. 2, 2014, Paper 027103. https://doi.org/10.1063/1.4864338

[26] Mulleners, K., Mancini, P., and Jones, A. R., "Flow Development on a Flat-Plate Wing Subjected to a Streamwise Acceleration," *AIAA Journal*, Vol. 55, No. 6, 2017, pp. 2118–2122. https://doi.org/10.2514/1.J055497

[27] Marzanek, M. F., and Rival, D. E., "Separation Mechanics of Non-Slender Delta Wings During Streamwise Gusts," *Journal of Fluids and Structures*, Vol. 90, Oct. 2019, pp. 286–296. https://doi.org/10.1016/j.jfluidstructs.2019.07.001

[28] Kim, D., and Gharib, M., "Flexibility Effects on Vortex Formation of Translating Plates," *Journal of Fluid Mechanics*, Vol. 677, April 2011, pp. 255–271. https://doi.org/10.1017/jfm.2011.82

[29] Vlachos, P. P., and Telionis, D. P., "The Effect of Free Surface on the Vortex Shedding from Inclined Circular Cylinders," *Journal of Fluids Engineering*, Vol. 130, No. 2, 2008, Paper 021103. https://doi.org/10.1115/1.2829578

[30] Lang, A. W., and Gharib, M., "Experimental Study of the Wake Behind a Surface-Piercing Cylinder for a Clean and Contaminated Free Surface," *Journal of Fluid Mechanics*, Vol. 402, Jan. 2000, pp. 109–136. https://doi.org/10.1017/S0022112099006722

[31] Chowdhury, J., Cook, L., and Ringuette, M. J., "The Vortex Formation of an Unsteady Translating Plate with a Rotating Tip," AIAA Paper 2019-0348, 2019. https://doi.org/10.2514/6.2019-0348

[32] Mueller, T. J., and DeLaurier, J. D., "Aerodynamics of Small Vehicles," *Annual Review of Fluid Mechanics*, Vol. 35, Jan. 2003, pp. 89–111. https://doi.org/10.1146/annurev.fluid.35.101101.161102

[33] Ol, M., and Babinsky, H., "Extensions of Fundamental Flow Physics to Practical MAV Aerodynamics," NATO Science and Technology Organization TR-AVT-202, Brussels, 2016.

[34] Dickson, W. B., and Dickinson, M. H., "The Effect of Advance Ratio on the Aerodynamics of Revolving Wings," *Journal of Experimental Biology*, Vol. 207, No. 24, 2004, pp. 4269–4281. https://doi.org/10.1242/jeb.01266

[35] Johnson, W., "Helicopter Theory," *Dover Books on Aeronautical Engineering*, Dover, New York, 2012, p. 128.

[36] Shumway, N., and Jones, A. R., "The Initial Growth of Normalized Circulation of the Leading-Edge Vortex on Surging and Rotating Wings," AIAA Paper 2020-0800, 2020. https://doi.org/10.2514/6.2020-0800

M. Smith
Associate Editor